

Programmable actuating systems based on swimming fiber robots

Hao Sun^{a,1}, Meng Liao^{a,c,1}, Jianfeng Li^a, Chao Zhou^b, Jue Deng^a, Xuemei Fu^a,
Songlin Xie^a, Bo Zhang^a, Yizheng Wu^b, Bingjie Wang^{a,c}, Xuemei Sun^{a,c},
Huisheng Peng^{a,c,*}

^a State Key Laboratory of Molecular Engineering of Polymers and Department of Macromolecular Science, Fudan University, Shanghai 200438, China

^b State Key Laboratory of Surface Physics, Department of Physics and Collaborative Innovation Center of Advanced Microstructures, Fudan University, Shanghai 200438, China

^c Laboratory of Advanced Materials, Fudan University, Shanghai 200438, China

ARTICLE INFO

Article history:

Received 27 February 2018

Received in revised form

16 June 2018

Accepted 24 June 2018

Available online 26 June 2018

Keywords:

Carbon nanotube

Microrobot

Actuating system

Self-propulsion

ABSTRACT

Microrobotics represents an important branch of robotics in the past decade, and demonstrates great potential in a broad range of applications such as targeted drug delivery, cell manipulation and bio-imaging. However, it is rare while becomes critical to make integrated and programmable actuating systems with sophisticated and controllable architectures that are demanded for real applications. Here, we present a new family of bio-inspired programmable actuating systems assembled from carbon nanotube/platinum swimming fiber robots (SFRs). The SFRs demonstrate hetero-sectional structures that offer rapid and stable rotations in H₂O₂ solution. Similar to the building blocks like tentacle and spine of invertebrates, the SFRs are then assembled into programmable actuating systems that may move in rotation and translation or switch between them. As a general and effective strategy, this assembling methodology may also open up a new direction for microrobotics on system level.

© 2018 Published by Elsevier Ltd.

1. Introduction

With the advance of light weight and miniaturization in robotics, considerable efforts have been devoted to developing microrobots with controllable structures such as microparticles/nanoparticles [1–7], nanotrees [8], microwires/nanowires [9–19] and bilayer structures [20]. However, these simplex structures cannot meet the requirements of real applications, e.g., it is difficult for them to effectively carry and move cargos. To this end, it is desiring to further make them into sophisticated while controlled architectures according to the different applications.

Nature may provide effective strategies for solve the above problem. For instance, through the formation of modular assembly, invertebrates such as starfish, jellyfish and urchin are capable to perform complex functionalities like food acquisition [21–24]. The integral architectures of the invertebrates are generally produced from various building blocks of tentacles and spines, which show

identical appearances, standard motion modes and independent neural units. These invertebrates in a system can then make effective movements *via* synergistic interactions among the building blocks.

Here, in mimicking the invertebrate, we present a new family of programmable actuating systems assembled from swimming fiber robots (SFRs). The SFR was made by modifying aligned multi-walled carbon nanotube (MWCNT) fibers with Pt nanoparticles *via* electrochemical deposition. Aligned MWCNT fibers were dry-spun from a spinnable MWCNT array synthesized by chemical vapor deposition. It is worth noting that as the skeleton of the actuating system, aligned MWCNT fibers simultaneously demonstrated high electrical conductivities of 10⁴–10⁵ S m⁻¹ and mechanical strengths of 10²–10³ MPa, which benefited the electrochemical modification process and the structural stability, respectively. Pt nanoparticles, as the catalyst for bubble-ejecting reaction to propel SFRs, were effectively deposited on fiber surfaces *via* a double potential step in K₂PtCl₆ solution. With the preparation process depicted in Fig. 1a, dual hetero-sectional structures were produced on one MWCNT fiber for self-propulsion (Fig. 1b and c, details in Experimental Section). Along the axial direction, one MWCNT fiber was divided into two different parts, i.e., Pt-deposited and bare MWCNT parts with the same length, between which the interface

* Corresponding author. Laboratory of Advanced Materials, Fudan University, Shanghai 200438, China.

E-mail address: penghs@fudan.edu.cn (H. Peng).

¹ These authors contributed equally to this work.

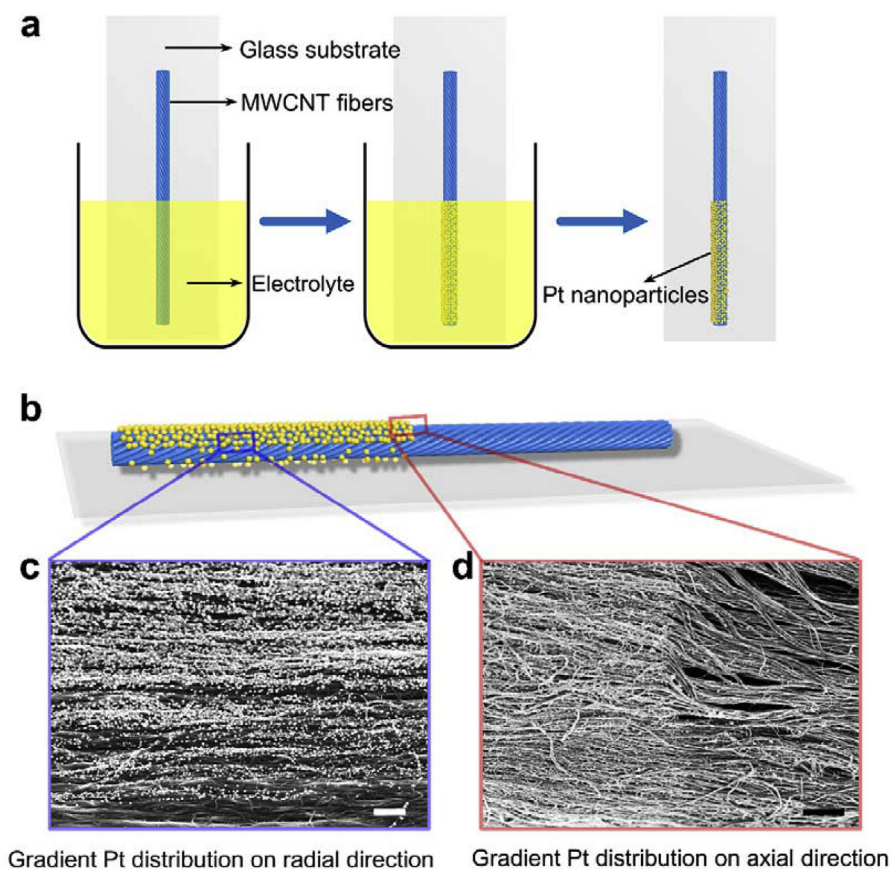


Fig. 1. Hetero-sectioned structure of the swimming fiber robot (SFR). (a) Schematic illustration to the preparation of SFRs based on electrochemical deposition. (b) Schematic illustration to the structure of the double-asymmetric-structured SFR. Radial dissymmetry, with blue box covering the denser and less Pt nanoparticles at the top and bottom; axial dissymmetry, with red box covering the bare MWCNT at the right and MWCNT/Pt at the left; respectively. (c) and (d), Scanning electron microscopy (SEM) images of the boundaries labelled at b. Scale bars, 1 μm . (A colour version of this figure can be viewed online.)

could be clearly observed under scanning electron microscopy (SEM) (Fig. 1c and S1). For the generation of rotatory movement, hetero-sectional Pt distribution on Pt-deposited part was realized by using a shadowing mask and electrolyte concentration gradient could thus result in gradient distribution of Pt in the radial direction (Fig. 1b and S2). The weight percentage of Pt could be controlled from 12 to 74.2% by varying the deposition cycles of the double-potential step.

2. Experimental section

2.1. Preparation of MWCNT fibers and $\text{Fe}_3\text{O}_4/\text{MWCNT}$ hybrid fibers

MWCNT fibers were dry-spun from spinnable MWCNT arrays. $\text{Fe}_3\text{O}_4/\text{MWCNT}$ hybrid fibers were prepared via a co-spinning process. Briefly, a three-layered MWCNT sheet was paved on a polytetrafluoroethylene panel prior to dropping Fe_3O_4 dispersion onto it. The MWCNT sheet was then scrolled into a fiber using a manual spinning machine with Fe_3O_4 nanoparticles wrapped inside by MWCNT bundles.

2.2. Hetero-sectional deposition of Pt nanoparticles

Electrochemical deposition was performed to incorporate Pt nanoparticles on the surface of MWCNT fiber. Briefly, aqueous solution containing 1 mM K_2PtCl_6 and 0.1 M KCl served as the electrolyte, and a standard three electrode setup was applied with a saturated Ag/AgCl and Pt electrodes as reference and counter

electrodes, respectively. A double-potential step method was conducted by setting the first step at 0.5 V for 10 s and the second step at 0.7 V for 10 s. MWCNT or $\text{Fe}_3\text{O}_4/\text{MWCNT}$ fibers were fixed on a glass slide with one side closely contacting the glass slide while the other side not, with electrode wire lead out by a commercial silver paste (SC666-80R, Uniwell). During electrochemical deposition, the liquid level of the electrolyte was required to be stably kept, ensuring a constant interface between Pt-deposited and bare MWCNT segments. When accomplished, the obtained fibers were washed with deionized water and dried in vacuum before use. SFRs with desired lengths can be obtained by cutting off the fiber with the same length above and below the liquid level.

3. Results and discussion

The rotation of a typical SFR was traced under dark-ground illumination (Fig. 2a and Movie S1). The SFR demonstrated a diameter of $\sim 20 \mu\text{m}$, length of 4 mm and Pt weight percentage of 74.2%, and it produced an angular speed of $\sim 9.7 \text{ rad s}^{-1}$ in 30 wt% H_2O_2 aqueous solution. Due to the bubbles generated by H_2O_2 decomposition at Pt-deposited section, a bright part on the SFR could be clearly observed. The bubbles appearing at the opposite side of the rotating direction further confirmed that the propulsion was generated by the counterforce of the ejecting bubbles. More detailed analysis on the angular speed was given in Note S5. Briefly, a driving torque (referred as τ_{dr}) is generated by oxygen release that results in the rotation of an SFR, while a resisting torque (referred as τ_{re}) exists due to the fluid viscosity of the solution. When an SFR

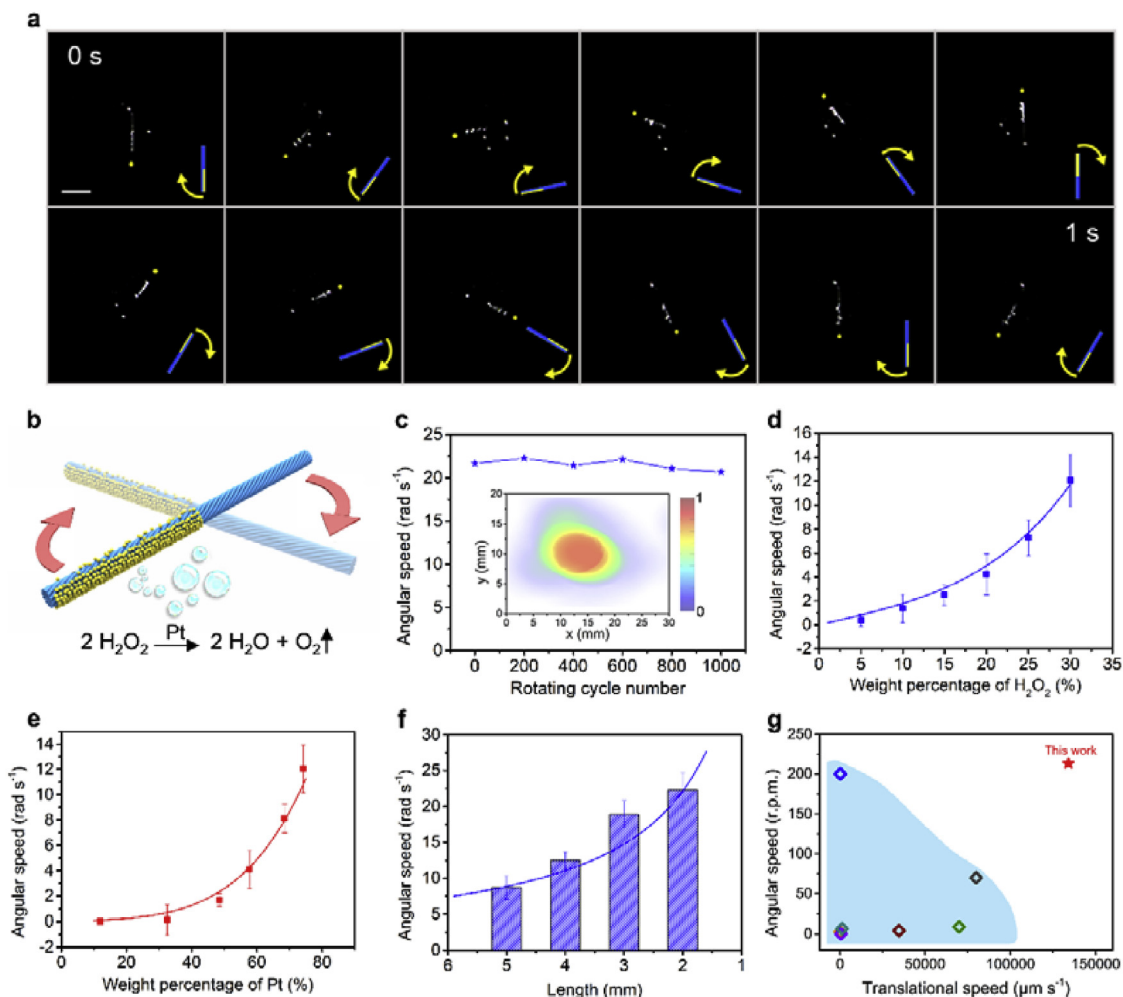


Fig. 2. Actuating properties of the SFR. (a) Photographs of a rotating SFR, each frame portrayed an advancement of 0.1 s from the left to the right. Scale bar, 2 mm. (b) Schematic illustration to the actuating mechanism and rotary movement of the SFR. (c) The variation of angular speeds in 1000 rotating cycles (inserted, heat map that demonstrated the deviation of mass center during rotation). (d), (e) and (f) Dependence of angular speed on H_2O_2 weight percentage, Pt weight percentage and total length of SFR, respectively. Pt weight percentage and total length of SFR were 74.2% and 4 mm at d, respectively. Total length of SFR and H_2O_2 weight percentage were 4 mm and 30% at e, respectively. Pt weight percentage of SFR and H_2O_2 weight percentage were 74.2% and 30% at f, respectively. (g) Comparison on the angular and translational speeds of previously reported swimming robots and the SFR in this work (from left to right, Ref 6, 3, 2, 1, 23, 24 and 25). (A colour version of this figure can be viewed online.)

was at first placed in H_2O_2 solution, τ_{dr} surpassed τ_{re} to produce an increasing angular speed. As τ_{re} increased positively correlated to speed, the SFR could finally achieve a stable rotation state within several seconds when τ_{re} was equal to τ_{dr} . To confirm that, we carefully investigated the angular speed of an SFR within one rotating circle frame by frame (Figure S4). As expected, similar angular speeds of $\sim 22.3 \text{ rad s}^{-1}$ were demonstrated during the traced cycle (Figure S5). To further verify the long-term stability, the angular speed of the SFR was recorded during 1000 rotating cycles, and 95.4% of the initial value was maintained (Fig. 2c). Furthermore, the center of the SFR was stabilized within a tiny area during 1000 rotating cycles (inserted heat map in Fig. 2c), indicating a steady rotatory behavior favored for modular assembly afterwards.

Supplementary video related to this article can be found at <https://doi.org/10.1016/j.carbon.2018.06.056>.

The dependence of angular speed on several key parameters, e.g., Pt weight percentage, length and H_2O_2 concentration had been systematically investigated. During steady rotation, the net driving torque produced by catalytic reaction is balanced by the drag torque due to the friction. The linear velocity (v_0) could be calculated by the following equation:

$$v_0 = F_{dr}/N\zeta$$

where F_{dr} , N and ζ referred to the net driving force, total number of the length element and friction coefficient of each length element, respectively. According to the equation, the angular speed increases with the increasing F_{dr} , which can be caused by the increasing fuel concentration and Pt weight percentage (detailed calculation provided in Notes S4 and S6). For instance, when an SFR (diameter of $\sim 12 \mu\text{m}$, length of 4 mm and Pt weight percentage of 74.2%) was rotating in H_2O_2 aqueous solution at increasing concentrations from 5 to 30 wt%, the angular speeds increased from 0 to 22.3 rad s^{-1} accordingly (Fig. 2d). Similarly, the angular speed also increased with increasing Pt weight percentages of the SFR, ascribing to more generated bubbles that promoted F_{dr} (Fig. 2e). With the increasing Pt weight percentages from 12% to 74.2%, the angular speeds increased from 0 to 12.4 rad s^{-1} accordingly. More detailed analysis on the dependence of angular speed on detached bubble diameter was provided in Figure S6 and Note S6. Decreasing on the fiber length (N) could also enhance the angular speed due to a lower linear velocity that reduced τ_{re} . For instance, decreasing fiber lengths from 4 to 2 mm resulted in increased angular speeds

from 8.7 to 22.3 rad s^{-1} (Fig. 2f). Note that this strategy was also effective to realize similar actuation behaviors using other fiber materials (e.g., graphene fiber and carbon fiber) modified with Pt nanoparticles (Movie S4).

Supplementary video related to this article can be found at <https://doi.org/10.1016/j.carbon.2018.06.056>.

Another interesting feature of these SFRs lied in the feasibility of multiple driving sources that enabled more complex and controllable movements. Magnetic responsiveness had been here investigated as a demonstration for multiple driving actuations. More specifically, superparamagnetic Fe_3O_4 nanoparticles were synthesized and incorporated to introduce magnetic-field driving for SFRs via a co-spinning process (Figure S10). The uniform distribution of Fe_3O_4 nanoparticles was verified by SEM and energy dispersive spectroscopy (EDS) (Fig. 3a–c), which showed no obvious influence on Pt deposition in the following step. The Fe_3O_4 -incorporated SFRs demonstrated high responsiveness in magnetic field, which achieved a velocity up to 134 mm s^{-1} (~24 body length per second) in a 2500 Oe magnetic field (Figures S11, S12 and Movie S5). Due to the existence of both Fe_3O_4 and Pt, the resultant SFR could be simultaneously driven by chemical fuel and magnetic field (Movie S6). Without magnetic field, the SFR rotated continuously, and when conducting the magnetic field, it could rapidly navigate along programmable paths as demonstrated in Fig. 3d and Movie S6. To the best of our knowledge, few reports have realized multimodal

movements on one single microrobot (Table S1). In comparison to most previous reports that realized two motion modes by re-designing and fabricating different structures of microrobots, the monolith SFR in our work could synchronously rotate and navigate straight forward. As a demonstration, a single SFR in our work demonstrated synchronous rotatory and translational movements on the basis of ejecting bubbles generated by H_2O_2 decomposition, as well as the interaction with magnetic field, achieving remarkable angular and translational speeds of up to 213.1 rpm and 134 mm s^{-1} respectively (Fig. 2g) [3–5,8,25–27]. It should be noted that other stimuli-responsive components can be also incorporated to introduce a broader range of driving sources for the SFRs, which may provide a general strategy for the development of intelligent microrobots.

Supplementary video related to this article can be found at <https://doi.org/10.1016/j.carbon.2018.06.056>.

The stable, predictable and controllable rotation behaviors of the SFRs pave the way for the further assembly into programmable actuating systems with customized configurations and motions. As a demonstration, we mainly focus on SFRs at millimeter scale, which bridges actuating systems between macroscopic and microscopic scale due to the dominant viscous effect that renders most machining strategies ineffective, requiring actuating systems with comprehensively high performances [25,26]. Herein, a variety of programmable actuating systems were prepared by assembling

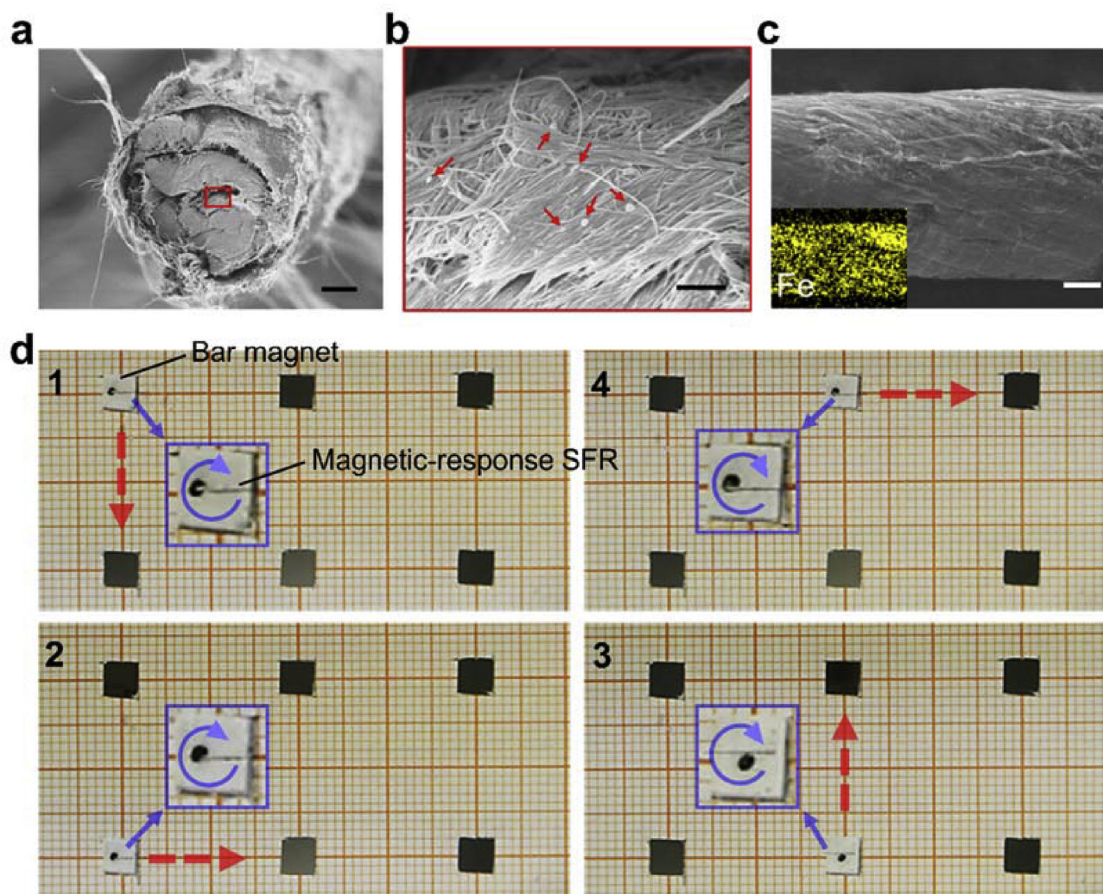


Fig. 3. Magnetic-response SFRs. (a) and (b), SEM images from sectional view of Fe_3O_4 -incorporated SFR at low and high magnifications, respectively. The red arrows at **b** indicate the presence of Fe_3O_4 superparamagnetic nanoparticles. (c) SEM image from side view of an SFR incorporated with Fe_3O_4 nanoparticles. Inserted, EDS image of Fe element. (d) A magnetic-response SFR simultaneously driven by magnetic field and chemical fuel. Rotation driven by chemical fuel: the modified SFR (indicated in a blow up blue box) constantly rotated on the surface of H_2O_2 solution. Translation driven by magnetic field: a bar magnet (the white part marked in **d**₁) was used and moved to guide the modified SFR navigated along a pre-designed trail marked with red arrows in **d**₁ to **d**₄. The photograph images were obtained from Movie S6. Scale bars, 10 μm at **a** and **c**, 500 nm at **b**, and 1 cm at **d**. (A colour version of this figure can be viewed online.)

identical SFRs into various configurations (Fig. 4). The different structures were prepared through connecting tail ends of SFRs in a pre-designed manner by ethyl-alpha-cyanoacrylate instantaneous adhesive. Aligned MWCNT fibers that are lightweight and mechanically strong contributed to a high structural stability of the resulting actuating systems. Twenty actuating systems with different configurations were assembled and then divided into two groups, i.e., rotation and translation, according to pre-designed motion modes. To be more specific, ten rotatory actuating systems were designed by making the driving torques of all the SFRs towards the same rotating direction (Fig. 4a). As for the translation group, ten actuating systems were assembled using equal number of SFRs with opposite driving torques (Fig. 4b). As expected, the reconfigurable actuating system processed the as-designed rotating or translation directions (Fig. 4c–h, Movie S7). On the

other hand, by manipulating the assembly strategies of SFRs, the actuating systems with the same geometry can display different motion modes, verifying the high adaptability of these actuating systems (Fig. 4e and f). Simulation on the motion behaviours of the above actuating systems also showed a good match with the experimental results (Notes S7, S8 and Figures S8 and S9). This bio-inspired assembling strategy could enable the realization of programmable actuating systems with more sophisticated motion modes, e.g., switchable rotation and translation movements. It may largely promote the single motion mode of previous microrobots, and thus represent a promising direction for the next-generation microrobots that can perform more sophisticated tasks on demand. To meet that goal, the basic building blocks are required to be tough enough to maintain the structural stability during transformation of the motion mode. Besides, they are expected to share

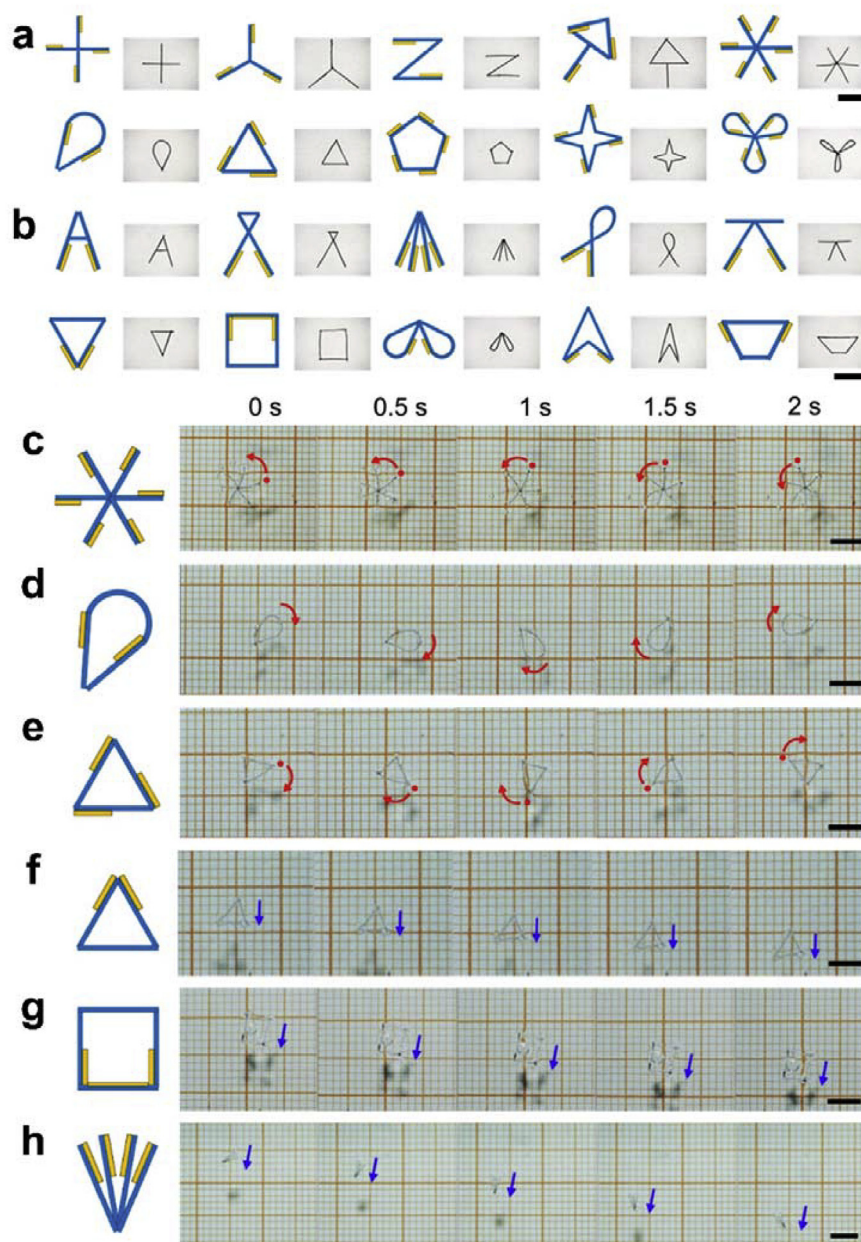


Fig. 4. Assembled SFRs showing tunable motions. (a) and (b) 20 assembled SFRs divided into rotating and translation motion groups, respectively. (c)–(h) Typical assembled SFRs showing rotating and translation motions (the leftmost panel as the configuration illustration and the right reconfigurable images at continuous moving states). The reconfigurable images were obtained from Movie S7. Scale bars, 5 mm. (A colour version of this figure can be viewed online.)

simple preparation processes and components that are beneficial for scale-up production. As a demonstration, a motion-mode-switchable actuating system was fabricated with a three-dimensional configuration (Fig. 5a). Two bare MWCNT fibers served as the fixed axis (G_0) for mode switching, and four SFRs were divided into two groups referred as G_1 and G_2 , which corresponded to rotation and translation modules, respectively (Fig. 5b and c). By selectively placing different planes (i.e., G_0/G_1 and G_0/G_2) on the surface of H_2O_2 solution before or during movement, the motion mode of the system could be reversely switched between rotation and translation modes (Fig. 5d and e, Movie S8).

Supplementary video related to this article can be found at <https://doi.org/10.1016/j.carbon.2018.06.056>.

The untethered actuating mobility can be inherited when assembled into 3D structures for moving small-scale cargos on the liquid interface, which remains challenging especially when high device integration is required. Here a three-dimensional fish-like actuating system was constructed using six SFRs as the module, while 5 in-plane and 3 vertical MWCNT fibers as the structural and loading modules, respectively (Fig. 5f). A piece of green graphene aerogel cargo (~ 40 mg, more than 10 times of the actuating system) was placed on the loading modules (Fig. 5g), and the fish-like actuating system navigated linearly on the solution by carrying the cargo on top (Fig. 5h, Movie S9). Although the propelling of SFRs is still dependent on H_2O_2 , as a general actuating strategy, the actuation can be potentially realized in other liquid systems sharing a surface tension propelled mechanism involving various forms

such as catalytic reactions, interfacial reactions and exfoliating particles. This feature may be rather promising in microfluidics, drug delivery and miniature robotics.

As the basic building blocks, SFRs demonstrated several remarkable features that were favored in assembly of complex actuating systems. The alignment of MWCNTs contributed both high tensile strength and electrical conductivity, enabling both high structural stability and deposition controllability of the SFRs; the combination of lightweight MWCNT (~ 0.633 mg cm^{-3}) and uniform Pt nanoparticles provided remarkable angular and translation speeds of ~ 213.1 rpm (during 1000 stable rotating cycles) and 134 mm s^{-1} , respectively. The primary SFRs can be assembled into 20 secondary assemblies with a broad range of architectures and desired motion modes, and the combination of secondary assemblies can even create three-dimensional architectures that enabled a dynamic switch between rotatory and translational movements, which had rarely been realized (Table S1).

4. Conclusions

In summary, we have developed programmable actuating systems with tunable architectures assembled from standardized SFRs, and these actuating systems may perform desired motion modes to effectively deliver cargos. As a general strategy, the assembling methodology also represents an important step towards system-level actuators, and provided inspirations for the development of the next-generation microrobots.

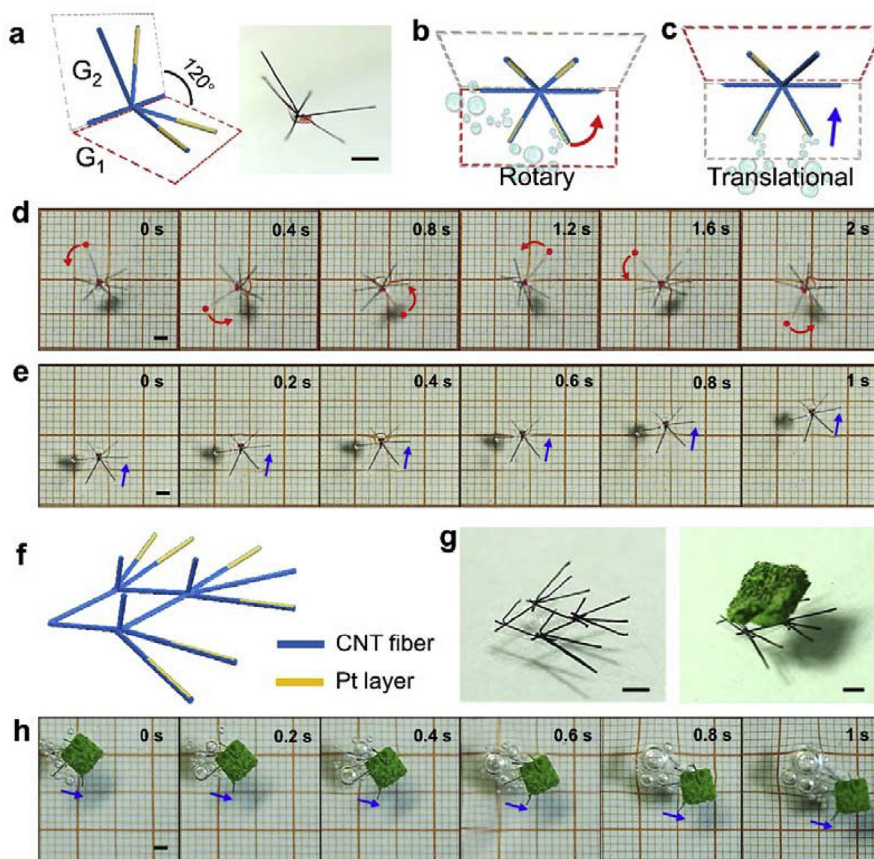


Fig. 5. Programmable actuating systems from SFRs. (a) Schematic illustration and photograph of a three-dimensional, motion mode-switchable system. (b) and (c) Schematic illustrations to rotating and translation modes of the actuating system at a, respectively. (d) and (e) Rotation and translation of the actuating system at a with G_1 and G_2 faces contacting the liquid, respectively. The red dots at d are labelled for the clarification in tracing the movement. (f) Schematic illustration to a three-dimensional fish-like actuating system. (g) Photographs of the actuating system at f without (left image) and with (right image) a cargo. (h) Navigating trajectory of the cargo-loaded actuating system at g. Scale bars, 2 mm. Diameters of the SFRs at a and g, ~ 65 μm . (A colour version of this figure can be viewed online.)

Acknowledgements

This work was supported by Ministry of Science and Technology of China (2016YFA0203302), National Natural Science Foundation of China (21634003, 51573027, 51403038, 51673043, 21604012) and Science and Technology Commission of Shanghai Municipality (16JC1400702, 15XD1500400, 15JC1490200).

Appendix A. Supplementary data

Supplementary data related to this article can be found at <https://doi.org/10.1016/j.carbon.2018.06.056>.

Supplementary video related to this article can be found at <https://doi.org/10.1016/j.carbon.2018.06.056>.

References

- [1] R.F. Ismagilov, A. Schwartz, N. Bowden, G.M. Whitesides, Autonomous movement and self-assembly, *Angew. Chem. Int. Ed.* 41 (2002) 652–654.
- [2] J.M. Catchmark, S. Subramanian, A. Sen, Directed rotational motion of microscale objects using interfacial tension gradients continually generated via catalytic reactions, *Small* 1 (2005) 202–206.
- [3] S.T. Chang, V.N. Paunov, D.N. Petsev, O.D. Velev, Remotely powered self-propelling particles and micropumps based on miniature diodes, *Nat. Mater.* 6 (2007) 235–240.
- [4] G. Loget, A. Kuhn, Electric field-induced chemical locomotion of conducting objects, *Nat. Commun.* 2 (2011) 535–540.
- [5] M. Kaynak, A. Ozcelik, A. Nourhani, P.E. Lammert, V.H. Crespi, T.J. Huang, Acoustic actuation of bioinspired microswimmers, *Lab a Chip* 17 (2017) 395–400.
- [6] J. Simmchen, J. Katuri, W.E. Uspal, M.N. Popescu, M. Tasinkevych, S. Sánchez, Topographical pathways guide chemical microswimmers, *Nat. Commun.* 7 (2016) 10598–10606.
- [7] R. Dong, Q. Zhang, W. Gao, A. Pei, B. Ren, Highly efficient light-driven TiO₂-Au Janus micromotors, *ACS Nano* 10 (2015) 839–844.
- [8] B. Dai, J. Wang, Z. Xiong, X. Zhan, W. Dai, C.C. Li, et al., Programmable artificial phototactic microswimmer, *Nat. Nanotechnol.* 11 (2016) 1087–1092.
- [9] L. Qin, M.J. Banholzer, X. Xu, L. Huang, C.A. Mirkin, Rational design and synthesis of catalytically driven nanorotors, *J. Am. Chem. Soc.* 129 (2007) 14870–14871.
- [10] Y. Wang, S.T. Fei, Y.M. Byun, P.E. Lammert, V.H. Crespi, A. Sen, et al., Dynamic interactions between fast microscale rotors, *J. Am. Chem. Soc.* 131 (2009) 9926–9927.
- [11] S. Sanchez, A.A. Solovev, S.M. Harazim, O.G. Schmidt, Microbots swimming in the flowing streams of microfluidic channels, *J. Am. Chem. Soc.* 133 (2011) 701–703.
- [12] S. Palagi, A.G. Mark, Y.R. Shang, M. Kai, Q. Tian, Z. Hao, et al., Structured light enables biomimetic swimming and versatile locomotion of photoresponsive soft microrobots, *Nat. Mater.* 15 (2016) 647–654.
- [13] T. Mirkovic, M.L. Foo, A.C. Arsenault, S. Fournierbidoz, N.S. Zacharia, G.A. Ozin, Hinged nanorods made using a chemical approach to flexible nanostructures, *Nat. Nanotechnol.* 2 (2007) 565–569.
- [14] U.K. Demirok, R. Laocharoensuk, K.M. Manesh, J. Wang, Ultrafast catalytic alloy nanomotors, *Angew. Chem. Int. Ed.* 120 (2008) 9489–9491.
- [15] R. Laocharoensuk, J. Burdick, J. Wang, Carbon-nanotube-induced acceleration of catalytic nanomotors, *ACS Nano* 2 (2008) 1069–1075.
- [16] K. Kim, X. Xu, J. Guo, D.L. Fan, Ultrahigh-speed rotating nano-electromechanical system devices assembled from nanoscale building blocks, *Nat. Commun.* 5 (2014) 3632–3640.
- [17] W. Wang, L.A. Castro, M. Hoyos, T.E. Mallouk, Autonomous motion of metallic microrods propelled by ultrasound, *ACS Nano* 6 (2012) 6122–6132.
- [18] D. Kagan, M.J. Benchimol, J.C. Claussen, E. Chuluun Erdene, S. Esener, J. Wang, Acoustic Droplet Vaporization and propulsion of perfluorocarbon-loaded microbullets for targeted tissue penetration and deformation, *Angew. Chem. Int. Ed.* 51 (2012) 7637–7640.
- [19] J. Li, T. Li, T. Xu, M. Kiristi, W. Liu, Z. Wu, et al., Magneto-acoustic hybrid nanomotor, *Nano Lett.* 15 (2015) 4814–4821.
- [20] P. Xiao, N. Yi, T. Zhang, Y. Huang, H. Chang, Y. Yang, et al., Construction of a fish-like robot based on high performance graphene/PVDF bimorph actuation materials, *Adv. Sci.* 3 (2016) 1500438–1500443.
- [21] N. Huebsch, D.J. Mooney, Inspiration and application in the evolution of bio-materials, *Nature* 462 (2009) 426–432.
- [22] P. Fratzl, F.G. Barth, Biomaterial systems for mechanosensing and actuation, *Nature* 462 (2009) 442–448.
- [23] K.K. Smith, W.M. Kier, Trunks, Tongues, and tentacles: moving with skeletons of muscle, *Am. Sci.* 77 (1989) 28–35.
- [24] G. Sumbre, Y. Gutfreund, G. Fiorito, T. Flash, B. Hochner, Control of octopus arm extension by a peripheral motor program, *Science* 293 (2001) 1845–1848.
- [25] J.G. Gibbs, Y.P. Zhao, Design and characterization of rotational multicomponent catalytic nanomotors, *Small* 5 (2009) 2304–2308.
- [26] D. Okawa, S.J. Pastine, A. Zettl, J.M. Fréchet, Surface tension mediated conversion of light to work, *J. Am. Chem. Soc.* 131 (2009) 5396–5398.
- [27] F. Meng, W. Hao, S. Yu, R. Feng, Y. Liu, F. Yu, et al., Vapor-enabled propulsion for plasmonic photothermal motor at the liquid/air interface, *J. Am. Chem. Soc.* 139 (2017) 12362–12365.